The role of laser wavelength on plasma generation and expansion of ablation plumes in air

A. E. Hussein,[1,2] P. K. Diwakar,[1] S. S. Harilal,[1] and A. Hassanein[1]
[1]*Center for Materials under Extreme Environment, School of Nuclear Engineering, Purdue University, West Lafayette, Indiana 47907, USA*
[2]*Department of Physics, McGill University, Montreal, Quebec H3A 0G4, Canada*

(Received 17 December 2012; accepted 26 March 2013; published online 10 April 2013)

We investigated the role of excitation laser wavelength on plasma generation and the expansion and confinement of ablation plumes at early times (0–500 ns) in the presence of atmospheric pressure. Fundamental, second, and fourth harmonic radiation from Nd:YAG laser was focused on Al target to produce plasma. Shadowgraphy, fast photography, and optical emission spectroscopy were employed to analyze the plasma plumes, and white light interferometry was used to characterize the laser ablation craters. Our results indicated that excitation wavelength plays a crucial role in laser-target and laser-plasma coupling, which in turn affects plasma plume morphology and radiation emission. Fast photography and shadowgraphy images showed that plasmas generated by 1064 nm are more cylindrical compared to plasmas generated by shorter wavelengths, indicating the role of inverse bremsstrahlung absorption at longer laser wavelength excitation. Electron density estimates using Stark broadening showed higher densities for shorter wavelength laser generated plasmas, demonstrating the significance of absorption caused by photoionization. Crater depth analysis showed that ablated mass is significantly higher for UV wavelengths compared to IR laser radiation. In this experimental study, the use of multiple diagnostic tools provided a comprehensive picture of the differing roles of laser absorption mechanisms during ablation. © *2013 AIP Publishing LLC*. [http://dx.doi.org/10.1063/1.4800925]

I. INTRODUCTION

Pulsed laser ablation (PLA) has numerous applications making it an attractive area of fundamental research. Some of the applications of PLA include laser-induced breakdown spectroscopy (LIBS),[1–3] laser-ablation inductively coupled-plasma mass spectrometry (LA-ICP-MS)[4] elemental sensors, micromachining,[5] nanomaterial production,[6] pulsed laser deposition (PLD),[7] and light sources for lithography and microscopy.[8,9] In particular, LIBS and LA-ICP-MS have emerged as popular analytical tools in fields as diverse as geochemistry and medicine because of their powerful detection capabilities. Extensive studies have been carried out on the fundamental properties of laser ablation plumes to improve the analytical capabilities of LIBS and LA-ICP-MS; however, the underlying physics of laser ablation remains incompletely understood due to complex laser-matter as well as plasma-ambient interaction processes.[1,2,10] Many previous experiments have focused on the adiabatic expansion of the laser generated plasma in vacuum, despite the fact that most applications of PLA are performed in the presence of an ambient gas. The presence of an ambient gas dramatically affects the laser-target and laser plasma coupling, as well as plasma expansion features.

Laser ablation is very complex, involving many simultaneous processes during and following the laser pulse such as heat transfer, electron-lattice energy exchange, material melting and evaporation, plasma plume formation and expansion, laser energy absorption, etc.[11] In the presence of an ambient gas the complexity of laser ablation process is increased by the occurrence of shock waves and plume confinement.[12–14] Some of the processes happening during ns laser-matter interaction are depicted in Figure 1, which include laser absorption in the surface and material excitation, temperature rise and surface melting, ablation and plasma formation, laser-plasma interaction, shock wave formation, and finally, in cases with sufficiently high ambient pressure, plume collapse. All these processes can be broadly classified into three regimes separated by different time zones (shown in dotted lines in Figure 1): (i) laser-target and laser-plasma interaction occurring during the laser pulse, (ii) plasma expansion and confinement, and (iii) plume condensation. The characteristics of laser produced plasmas (LPPs) depend on numerous parameters, such as target material, laser wavelength, pulse duration, and irradiance, as well as ambient gas pressure and composition.[14,15] Previous studies into the effects of different processing wavelengths on laser ablation have shown differences in plasma threshold energies, electron densities, and ablation mechanisms.[9,16–21]

Analysis of LPP can be a very challenging task considering its transient nature as well as large variations in plasma properties with space and time. There are numerous diagnostic techniques[22] that can be employed to study the characteristics of laser ablation such as shadowgraphy,[12] interferometry,[23] self-emission imaging using fast gated cameras,[20] optical emission spectroscopy (OES),[24] Langmuir probe,[25] Faraday cup,[9] etc. Each plasma diagnostic tool has its own advantages and limitations and thus comprehensive insight lies in the consolidation of information gathered from many techniques. For example, shadowgraphy allows for the laser induced shock wave as well as abrupt changes in gaseous ablation products to be visualized,

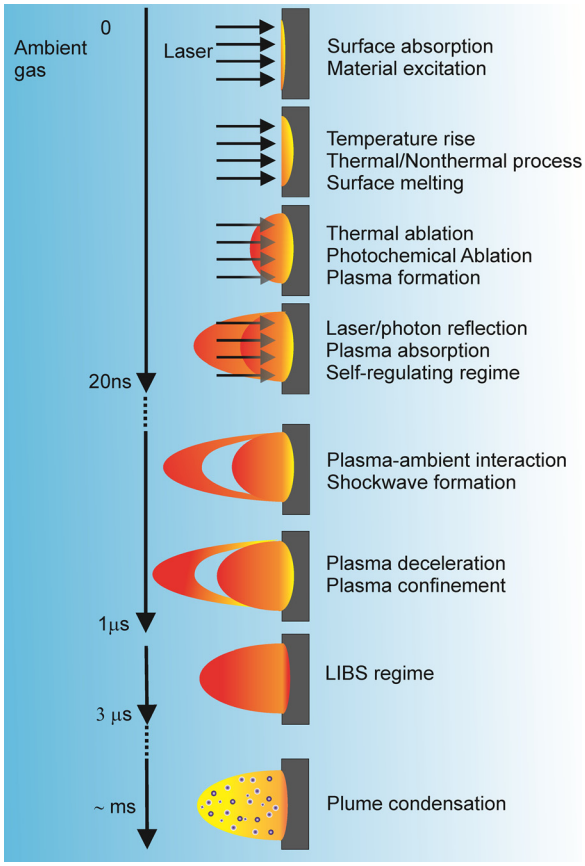

FIG. 1. Schematic of processes involved in ns laser ablation in 1 atmosphere air, with an approximate timeline of their occurrence.

providing information about the generation of shock fronts, internal plume structure, and material ejection.[12,26] Fast photography provides the details of the expansion dynamics of laser produced plasma plumes, especially in the presence of an ambient environment.[27–29] The OES allows information regarding the composition of a material through the analysis of recorded spectra, as well as estimation of fundamental parameters of the plasma.[10,24,30,31] Analysis of craters generated by laser ablation gives insight into ablation rate and efficiency, which is essential for understanding and controlling laser applications.[18,20,32] Using multiple diagnostics simplifies the task of characterizing the processes involved in laser ablation and strengthens the validity of results.

In this article, we report the role of laser excitation wavelength on plasma generation, laser-plasma coupling, plasma expansion dynamics and confinement, and crater generation. Plasmas were generated using 6 ns pulses from Nd:YAG laser emitting at its fundamental (1064 nm), second (532 nm), and fourth harmonics (266 nm), focused onto an aluminum target. We used a multitude of diagnostic techniques to fully understand the effect of wavelength on plasma generation and confinement at atmospheric pressure. The use of shadowgraphy, ICCD fast photography, optical emission spectroscopy, and crater analysis using white-light interferometry provided complementary information about the effects of excitation wavelength on laser-target and laser-plasma coupling.

II. EXPERIMENTAL DETAILS

For laser ablation, 1064 nm, 532 nm, and 266 nm wavelengths were used from an Nd:YAG laser with Gaussian profile full width at half maximum (FWHM) 6 ns. The fundamental frequency was doubled (532 nm) and quadrupled (266 ns) using KDP crystals and dichroic mirrors for frequency separation. The laser beam was focused onto the target using a plano-convex lens, producing a spot size of approximately 100 μm. Laser pulse energies of 12 mJ (153 J/cm^2), 25 mJ (318 J/cm^2), and 50 mJ (636 J/cm^2) were used. An aluminum slab of 2 mm thickness was used as the target. An X-Y translator provided a fresh ablation surface to avoid errors caused by local heating and drilling. All experiments were conducted in air at atmospheric pressure. The laser intensity at the target surface was varied using a combination of half wave plate and polarizing cube.

For performing focused shadowgraphy, Nd:YAG laser with 8 ns pulse duration and 532 nm wavelength was used as the probe beam. A charge coupled device (CCD) camera was used to capture the shadowgrams of laser-induced plasmas. The probe beam was synchronized to the camera and ablation beam using a timing generator, with a maximum temporal jitter of $\pm$ ns. The delay between the probe and ablation beams was varied to image the plasma plume at different times during its expansion. Increments of 2 ns delay were used until 40 ns, followed by 10 ns delays until 100 ns, and finally 100 ns delays until 600 ns, with 0 ns corresponding to the peak of the laser pulse. A 250 micrometer wire was used to calibrate the image size.

For fast photography, two-dimensional images of the plume intensity were captured on the ICCD camera. The ICCD camera was placed perpendicular to the laser beam, and a glass objective lens was used to image the plasma plume region onto the camera. Visible radiation from a wavelength range of 350–900 nm was recorded integrally from the plasma. A 2 ns gate width was used to image plasma at early times ($<$200 ns) and at later times a gate width of 10% of the sequential delay time was used. A shorter gate width was more desirable during early expansion times to minimize spatio-temporal mixing and optimize the imaging of internal structures. Plasma properties are no longer rapidly changing at later times; therefore, a longer gate width is acceptable and used to compensate for lesser emission at later times of plasma evolution.

For the OES, we used a triple grating 0.5 m spectrograph. An optical system consists of two lenses was used to image the plasma plume onto the entrance slit of the spectrograph. The spectrograph was coupled with an ICCD to detect the wavelength dispersed plasma emission in the visible range. Emission spectroscopic studies were performed perpendicular to the direction of plasma expansion. A programmable timing generator was used to synchronize the ICCD and the laser. For recording Stark broadened profiles of excited Al ionic lines, an 1800 lines/mm grating was used which provided a spectral resolution $\sim$0.025 nm.

A white light interferometry microscope was used to characterize the craters formed on the aluminum target. This apparatus allowed the morphology, depth and diameter of

craters produced by each wavelength and energy to be analyzed. The measured crater depth discussed in this study represents the maximum depth as measured by white light interferometry.

III. RESULTS

We used various diagnostic techniques to investigate the role of laser wavelength on plasma generation and confinement at one atmospheric air pressure. The diagnostic techniques used are shadowgraphy, ICCD fast photography, optical emission spectroscopy, and crater analysis using white-light interferometry, and they provide complementary information about the effects of excitation wavelength on laser-target and laser-plasma coupling. Shadowgraphy images correspond to second order of the refractive index field which reveals the inhomogeneities in the medium of interest and therefore follows shock wave front position generated by laser produced plasma. Fast photography images on the other hand measures plume's self-emission and thus provides two-dimensional snapshot of three-dimensional LPP plume propagation. Russo and co-workers[33,34] have studied in detail LPP shockwave and plume expansion dynamics using ICCD imaging and shadowgraphy when the plume expanded into three background gases (He, Ne, and Ar). Their studies highlighted complex interaction between the plume and ambient gas and the role of atomic mass of the background gas on laser-plasma interaction.[33,34] In the present article, we highlight the role of laser wavelength on plasma generation and its expansion dynamics. Plume morphologies and shockwave expansion dynamics are studied using fast photography and focused shadowgraphy, respectively, while optical emission spectroscopy is used to infer electron number density variation with time and white-light interferometry is used to measure crater depths.

A. Shadowgraphy

Laser ablation in the presence of an ambient gas leads to the generation of shock waves through the collisional interaction of expanding plume species and ambient gas atoms when the mass of the swept gas is greater than the mass of the ablated plasma.[23] Shadowgraphy allows for this shock wave as well as abrupt changes in gaseous ablation products to be visualized.[35] The laser-plasma generated shock wave contains valuable information about laser-material interaction, and thus its spatial and temporal analysis is of great interest in fundamental research. Figure 2 shows a typical progression of shadowgrams, illustrating the spatial and temporal evolutions of the ablation process and plume expansion into ambient air. Each time corresponds to the delay after the peak of the ablation beam; time delays between the ablation and probe beams were used to visualize the time evolution of the plasma plume. Opaque plumes at early times of expansion may be due to high electron densities, or spatio-temporal mixing of the plasma plume with the probe beam.[12]

Laser produced plasmas are characterized by steep changes in refractive index, as well as rapidly changing electron density,[33] which can clearly be viewed in shadowgrams. Information about pressure, temperature, and initial energy

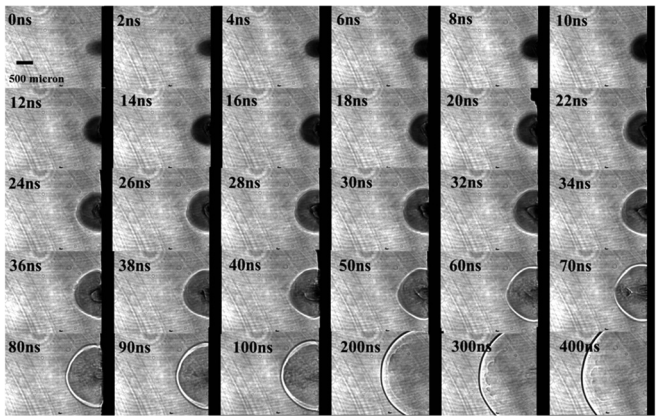

FIG. 2. Typical progression of shadowgrams of ns laser-induced plasma at increasing time delays in ambient air over an aluminum target. For generating plasma frequency doubled radiation from a Nd:YAG laser is focused on an Al target with a laser energy 50 mJ. The shadowgrams were recorded using 8 ns FWHM frequency doubled Nd:YAG laser. The times given in the frames correspond to times after the peak of the pump laser with respect to probe laser.

of the laser generated shock wave can be deduced from these images showing shock wavefront expansion by application of the analytical Taylor-Sedov solution to the point blast problem:[36]

$$R(t) = \varepsilon \left(\frac{E}{\rho}\right)^{\frac{1}{n+2}} t^{\frac{2}{n+2}}, \tag{1}$$

where ε is a constant dependent on specific heat capacity ratio, E is the energy released during explosion, ρ is the background gas density, and t is the delay time following ignition. The parameter n depends on the shape of the propagating shock wave; $n = 3$, 2, or 1 for spherical, cylindrical, or plane shock waves, respectively. Based on Choi *et al.*, the typical energy E released during explosion lies between 10% and 15% of the input laser pulse energy.[37]

The spatio-temporal evolution of LPP shock wave front at each wavelength were compared with the spherical ($n = 3$) Taylor-Sedov solution at various fluences for 266 nm, 532 nm, and 1064 nm laser excitation and are given in Figure 3. The spherical solution was in good agreement for all wavelengths studied at lower energies (12 mJ and 25 mJ). However, we noticed disparities in the spherical Taylor-Sedov fittings at higher energies, especially for longer wavelengths. Although the spherical fits for 1064 nm were in good agreement with experimental data for lower energies (12 and 25 mJ), significant deviations were observed after 50 mJ for early times of plasma evolution. Deviations from the spherical blast wave solution at higher energies for 1064 nm may indicate that the shock wavefront and associated plume features were more cylindrical when created by 1064 nm pulses.

According to Figure 3, the disagreement with spherical Taylor-Sedov equation is more pronounced at early times of plasma generation at higher energies and longer wavelengths. We examined the plasma properties at the peak of the laser pulse at different energies. Figure 4 gives the shadowgrams recorded at the peak of the laser pulse (0 ns) for all

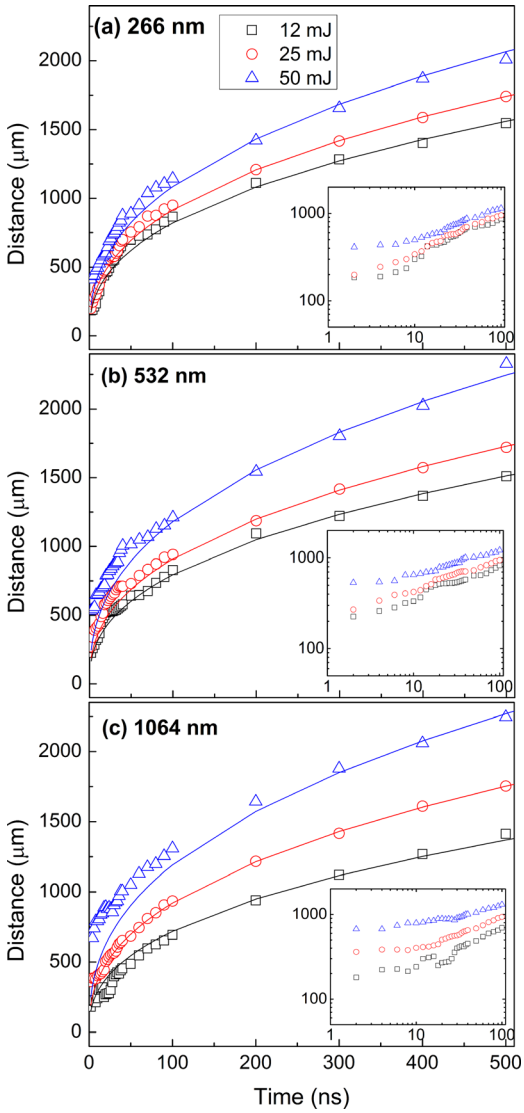

FIG. 3. R-T plots obtained from shadowgraphic images are given for (a) 266 nm, (b) 532 nm, and (c) 1064 nm. The curve fittings correspond to spherical Taylor-Sedov solution to the point blast problem which show good agreement for 12 mJ and 25 mJ for all wavelengths studied. At higher energies, a deviation in fitting can be evident especially for longer wavelengths. The inset figure provides log-log plot illustration of the spatio-temporal evolution of the shockwave front at shorter delays. The times given in the figure correspond to times after the peak of the pump laser with respect to probe laser.

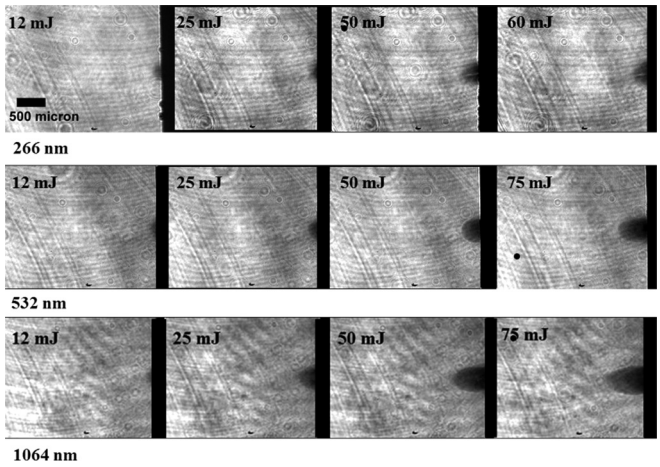

FIG. 4. Comparison of laser-induced plasmas for 266 nm, 532 nm, and 1064 nm wavelengths for various energies at the peak of the laser pulse. It is observed that plasmas are more cylindrical for higher wavelengths and energies.

laser excitations (1064 nm, 532 nm, and 266 nm) at various laser energies. As shown in Figure 4, plasma shock wavefronts are more cylindrical at higher energies, notably starting at 25 mJ, for 1064 nm wavelength. Shock wave front recorded at the laser peak for 532 nm wavelength are also cylindrical at higher energies, with the effect becoming obvious after 50 mJ. However, shadowgrams are found to be more spherical for 266 nm wavelength. This is consistent with position-time plots given in Figure 3.

The time evolution of shadowgrams recorded at 12 mJ laser energy is given for all laser excitation wavelengths studied in Figure 5. In this figure, it appears that shockwave front at lower laser energies is approximately spherical for all three wavelengths, with little discernible differences between shock wave structures. However, the time evolution of shadowgrams recorded at 50 mJ, given in Figure 6, shows noticeable differences in shock wavefront morphologies for different wavelengths. It is observed that 266 nm shadowgrams are darker and more spherical, while 1064 nm plumes appear less dense and are more cylindrical. A distorted structure on the tip of the external shockwave is also visible from very early times in the expansion of plasmas generated by 266 nm laser excitation.

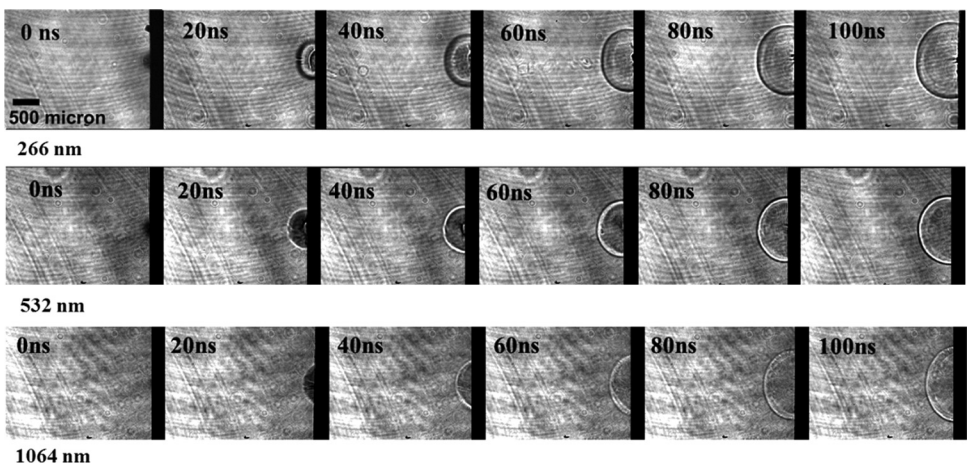

FIG. 5. Shadowgrams of 266 nm, 532 nm, and 1064 nm plasma shock wave expansion at 12 mJ. Plumes for all three wavelengths are spherical, indicating that the effect of wavelength on shock wavefront morphology is negligible at low energies.

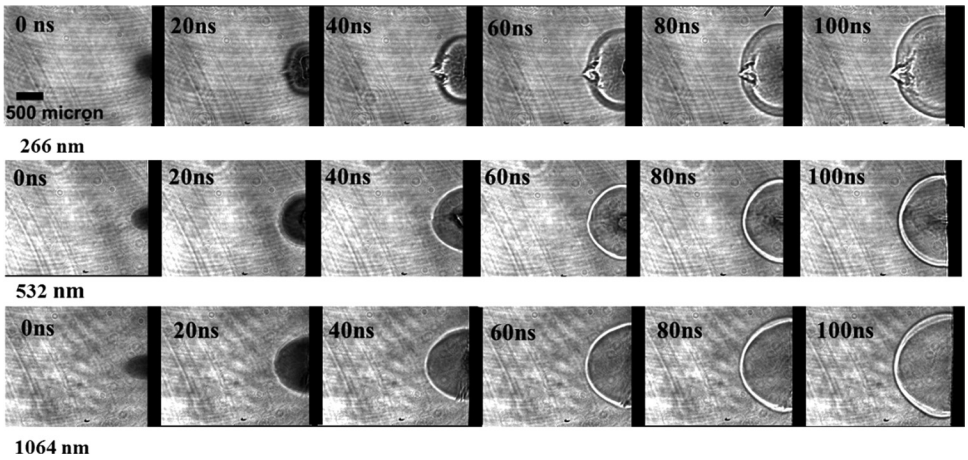

FIG. 6. Shadowgrams of 266 nm, 532 nm, and 1064 nm plasma shock wave expansion at 50 mJ. The dependence of wavelength on shock wavefront morphology is evident at higher energies.

B. Fast photography

Fast photography employing ICCD provides two-dimensional imaging of the expanding LPP plume. These images provide valuable insight into the hydrodynamic expansion of plasma plumes, as well as radiation emission. Typical ICCD images recorded at 30 ns after the peak of the laser pulse for different wavelengths and laser energies are shown in Figure 7. A gate width of 2 ns is used for obtaining these images and images are normalized to their maximum intensity obtained for 1064 nm for a given laser energy for better viewership. The colors in the ICCD camera images indicate different radiation intensity values. Higher counts observed in the images may correspond to areas of high temperature and particle density in the plasma plume. From these images it is obvious that laser wavelength has an influence on plume morphology at all energies (12 mJ, 25 mJ, and 50 mJ). Notable differences in plume morphology are even observed in ICCD images at 12 mJ, while shadowgraphy results showed little discernible difference in shock wavefront morphologies at low energy.

Figure 8 gives spatio-temporal evolution of 2 ns gated ICCD images for 1064 nm laser generated plasmas at laser energy of 25 mJ. Similar to shadowgrams, plasma confinement is evident in self-emission images. However, unlike the shock wavefront expansion observed in shadowgrams, a sharp boundary does not occur in ICCD imaged plumes. As the plasma expands, excited particles within the plasma collide with atmospheric particles, arresting its expansion into the environment and decreasing the kinetic energy of the plume which causes increased heating of the plasma plume and thus larger "hot spots" are observed in ICCD images. Position-time plots obtained from ICCD images are given in Figure 9 for 12 mJ pulse energy at 1064 nm, 532 nm, and 266 nm laser ablation. The R-t plots obtained from the fast photography are found to be distinctly different from shadowgraphic data both in trend and range. Fast photography data does not show a good fit with the blast model. The drag model has been shown to provide a good fit for plume expansion in ambient gas medium.[12] Figure 9 shows that the data fitted with the drag model shows a good correlation to some extent for 1064 nm case while it deviates considerably for 266 nm and 532 nm, especially at early times. In

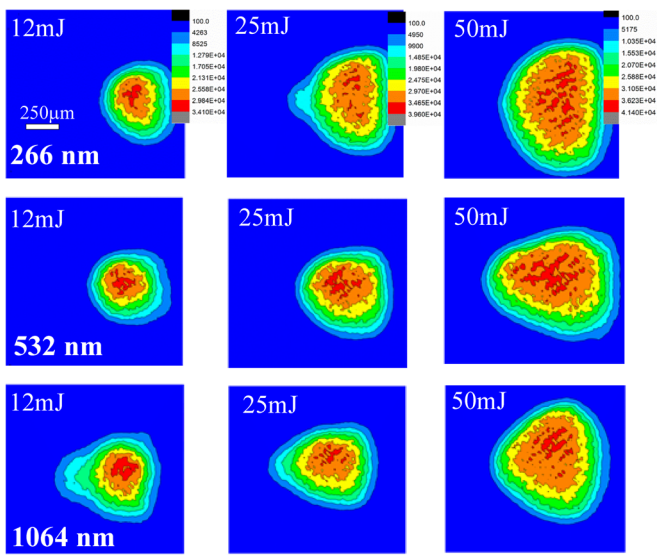

FIG. 7. Two-dimensional ICCD images showing plasma plume expansion and radiation for 266 nm, 532 nm, and 1064 nm pulsed laser ablation for three different energies recorded at 30 ns after the onset of plasma formation. Each image at a particular energy is normalized to maximum intensity with respect to 266 nm images of the same energy.

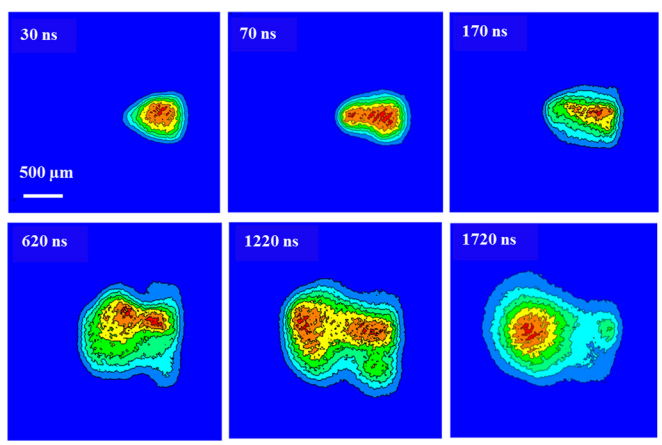

FIG. 8. Time sequence of fast photography images showing the spatio-temporal evolution of the plasma plume recorded during 1064 nm pulsed laser ablation at 25 mJ. The images are normalized to the peak intensity in that image for clarity.

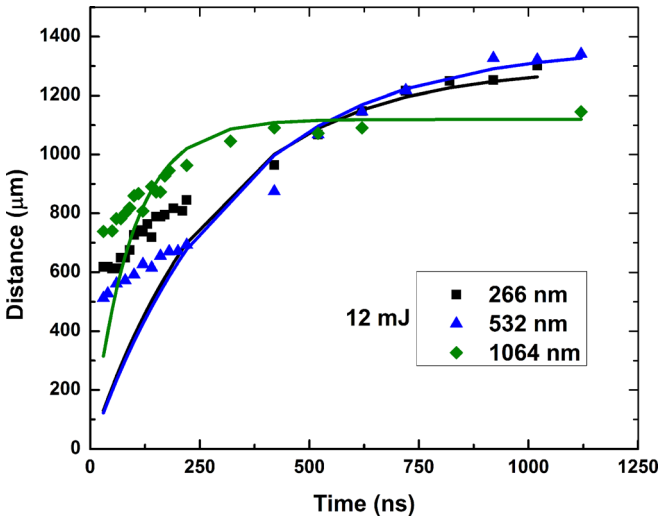

FIG. 9. Position-time plots obtained from ICCD images are given for 1064 nm, 532 nm, and 266 nm ablation for 12 mJ pulse energy. The best fits given in the figure are obtained using the drag model.

shadowgraphy, a distinct boundary is always seen in the interface between the shock wavefront and the background ambient. However, such a clear boundary is not seen in the ICCD images due to intense emission from the plume caused by confinement which may lead to errors in defining the edge. So laser plume hydrodynamic features obtained using ICCD imaging at high ambient pressures may not represent the plume boundaries accurately. Previous studies showed ICCD photography is more useful for understanding the hydrodynamics of the plume at low to moderate pressures (<1 Torr).[13]

C. Optical emission spectroscopy

Shadowgram and ICCD images clearly showed that the laser excitation wavelength affects plasma plume morphology. However, shadowgram images recorded at earliest times (first 20 ns) showed darkened regions without any structures for all excitation wavelengths studied. This could be due to high densities of the plasma at early time or spatial-temporal mixing of the probe and pump beam. The obscurity of shadowgram images for early times inhibits us from extracting information about fundamental parameters. Therefore, to obtain a better understanding of the fundamental parameters of plasma plumes we estimated the electron number density of laser ablation plumes using Stark broadening of isolated lines using OES.

The electron number density is an important plasma parameter, crucial to the understanding of plasma characteristics and establishing equilibrium status. In this experiment, the singly ionic Al spectral line at 281.62 nm was chosen for density estimation. A Lorentian profile was fitted to this Stark broadened spectral line, from which the FWHM was measured. The measured FWHM of this spectral line was corrected for instrument broadening to determine the FWHM to the Stark broadened profile using the following equation:[10]

$$\Delta\lambda_{measured} = \left(\frac{\Delta\lambda_{Stark}}{2}\right) + \sqrt{\left[\left(\frac{\Delta\lambda_{Stark}}{2}\right)^2 + (\Delta\lambda_{inst})^2\right]}, \quad (2)$$

where $\Delta\lambda_{measured}$ is the measured FWHM of the spectral line, $\Delta\lambda_{Stark}$ is the true FWHM of the Stark broadened line, and $\Delta\lambda_{inst}$ is instrumental broadening. Once the FWHM of the Stark broadened line is known, the electron number density can be calculated using:[38]

$$\Delta\lambda_{Stark} = 2\omega\left(\frac{N_e}{10^{16}}\right), \quad (3)$$

where ω is the impact factor and N_e is the electron number density. The impact factor is taken from Ref. 39.

Figure 10 shows the temporal evolution of electron number density for all three wavelengths at 12, 25, and 50 mJ recorded at a distance 1 mm from the target surface. Electron density measurements at early times (<30 ns) using

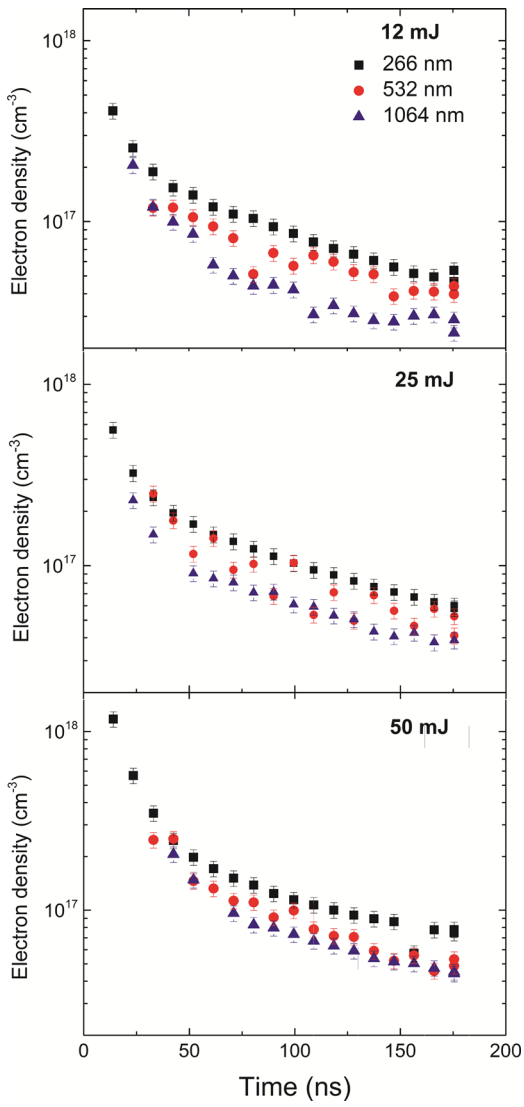

FIG. 10. Plots of electron density versus time for 12 mJ, 25 mJ, and 50 mJ comparing electron number density for the three wavelengths at each energy. The measurements are taken at 1 mm from the target surface.

OES are subject to inaccuracies caused by the presence of continuum and therefore are not given. The trend of electron number density for the three wavelengths was the same for all energies investigated. Irrespective of the excitation wavelength used, the temporal evolution of electron density showed a rapid drop due to expansion of the plume into the ambient atmosphere. The expanding plume eventually equilibrated with background pressure, creating this trend. By 200 ns, all three wavelengths at all energies have decayed to an electron number density of approximately $4 \pm 0.5 \times 10^{16}\,\mathrm{cm}^{-3}$.

The electron number density of plasmas generated with 1064 nm wavelength was consistently the lowest for all energies. As well, for all three energies, 266 nm laser ablation had the highest electron densities. It is observed that electron number density increases with increasing laser energy for all wavelengths. The highest electron density observed for 532 nm at 12 mJ is approximately $5.5 \times 10^{17}\,\mathrm{cm}^{-3}$, while the highest density at 50 mJ is approximately $1.2 \times 10^{18}\,\mathrm{cm}^{-3}$. Similarly, 266 nm plasmas have peak electron density of approximately $4.2 \times 10^{17}\,\mathrm{cm}^{-3}$ at 12 mJ and $\sim 1.18 \times 10^{18}\,\mathrm{cm}^{-3}$ at 50 mJ. Plasmas generated by 1064 nm pulses are least influenced by increased laser energy.

D. Laser ablation crater analysis

Studying ablation craters gives useful information about the ablation rate and efficiency for different wavelengths. We used a white-light interferometry microscope to measure the profile and depth (maximum crater depth) of laser ablation craters. Craters were created using five single shots onto a fresh surface of aluminum at 12 mJ, 25 mJ, and 50 mJ for 1064 nm and 266 nm laser wavelengths. The measured crater depths for 1064 nm and 266 nm wavelengths at different laser energies are given in Figure 11. It is obvious from this graph that crater depth increases with increasing fluence in the range of 12–50 mJ. This is consistent with the findings of Cristoforetti *et al.*,[40] who also studied laser ablation of an aluminum target in air. The measured crater depths are found to be increased with decreasing laser wavelength.

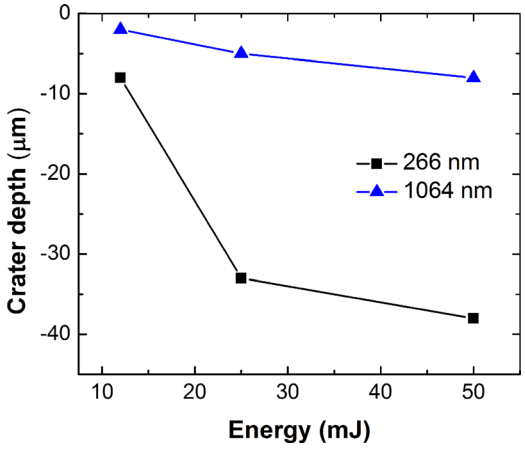

FIG. 11. Trend of crater depths for 266 nm and 1064 nm laser ablation at various laser energies.

IV. DISCUSSIONS

Noticeable differences in both radiation and kinetic properties of the plasmas generated by 1064 nm, 532 nm and 266 nm Nd:YAG laser excitation are seen through the comparison of shadowgrams, ICCD images, electron density estimates, and crater profiles. Through these analysis techniques it is obvious that excitation wavelength λ plays a crucial role in the properties of plasma generated by laser pulses. Previous studies showed that laser wavelength affects laser-target (mass ablation rate, penetration depth) and laser-plasma (absorption, reflection) coupling efficiencies, as well as optical properties of the plasma (opacity).[4,9,18,19,41]

As pictured in Figure 1, plasma initiation occurs immediately after laser arrival at the target surface. Following plasma initiation, two forms of coupling occur and influence subsequent plasma plume dynamics: laser-target and laser-plasma coupling. Laser-target coupling indicates more mass ablation, while increased laser-plasma coupling leading to reheating of the plume. The critical electron density plays an important role in the dynamics of plasma plume expansion, mediating between laser-target coupling and laser-plasma coupling. The critical density is the free electron density at which plasma oscillation frequency is equal to the laser frequency and it is given by:[22]

$$n_c = \frac{\pi m_e c^2}{e^2 \lambda^2} = \frac{10^{21}}{\lambda^2}\,\mathrm{cm}^{-3}, \tag{4}$$

where m_e is the electron mass, c is the speed of light, e is the electron charge, and λ is the laser wavelength. Governed by inverse wavelength squared proportionality, the critical electron density is lower for 1064 nm laser wavelengths ($n_c = 8.9 \times 10^{20}\,\mathrm{cm}^{-3}$) than for 266 nm ($n_c = 1.4 \times 10^{22}\,\mathrm{cm}^{-3}$). This means that plasma achieves the critical electron density more easily for IR light than UV laser excitation.

Shadowgrams recorded at the peak of the laser pulse in Figure 4 clearly show critical density effects. As shown in the figure, plasma shapes are more cylindrical at higher energies, notably starting at 25 mJ, for 1064 nm wavelength. Plasma shadowgrams recorded for 532 nm wavelength are also cylindrical at higher energies, with the effect becoming more obvious at higher energies. The plasmas are found to be more spherical for 266 nm wavelength. Deviations from the spherical Taylor-Sedov solution to the blast point problem for 1064 nm plasmas, shown in Figure 3, summarize the LPP expansion behavior, agreeing with shadowgram results observed at the peak of the laser pulse. Cylindrical shock wavefronts form as a result of increased laser-plasma coupling, increasing the thermal energy and subsequently kinetic energy of the plasma plume, causing it to expand from the target with higher velocity.

It is also observed that shock wavefronts at lower energies in Figure 4 are spherical for all wavelengths. This could be at lower energies the critical electron density is not achieved and therefore most of the laser energy goes for laser-target coupling. This point is further emphasized in a side by side comparison of shock wavefront evolution for each wavelength at 12 mJ and 25 mJ, as shown in Figures 5 and 6. In Figure 5, the wavelength effect is negligible for

12 mJ laser energy. All plasmas generated by various laser wavelengths expand similarly at low energies because the majority of laser energy is used for target heating and ablation. The wavelength effect is obvious in Figure 6, where 266 nm plumes are darker and more spherical, indicating greater laser-target coupling, while 1064 nm plumes are more cylindrical and appear less dense, consistent with higher laser-plasma coupling. This fact is also supported by crater analysis where deeper craters are noticed for shorter wavelength excitation. Opaque plumes at early times of expansion may be due to high electron densities, or spatio-temporal mixing of the plasma plume with the probe beam. Effects of spatio-temporal mixing in the shadowgram could be minimized by using a probe with shorter pulse probe beam. In present experiment, the FWHM of the probe beam used is 8 ns.

A distorted structure on the tip of the external shockwave is visible for 266 nm LA which could be due to the formation of laser supported detonation (LSD).[34,42] Because of higher photon energies of UV lasers, the compressed gas layer may absorb the incoming laser pulse and can generate a sustaining LSD wave during the laser pulse duration. LSD stops propagating by the end of laser pulse, but due to non-uniform heating, the central tip of the vapor plume and adjacent shockwave continue to move faster than rest of the plume, resulting in the formation of a bumpy structure on the top of the external shockwave, as seen in the shadowgrams.

Although laser-target coupling is expected to be higher for shorter wavelengths, the reported plasma ignition threshold is found to be higher for UV wavelengths compared to visible or IR wavelengths.[43] The reported values of plasma ignition threshold for Al target using 1064 nm, 532 nm, and 266 nm are 1.01, 1.30, and 3.64 J/cm^2, respectively.[43] The differences in plasma ignition threshold with laser excitation wavelength could be caused by various laser energy absorption mechanisms. There are three main mechanisms of laser energy absorption: electron-ion inverse Bremsstrahlung, electron-neutral inverse Bremsstrahlung, and photoionization. The probability of electron-ion IB process is much greater than that by electron-neutral, except in the very early stages of the laser evaporation process, and thus electron-neutral IB is generally considered negligible during laser ablation processes.[43,44] The inverse bremsstrahlung absorption α_{ib} via free electrons is approximated by[45]

$$\alpha_{ib} = 1.37 \times 10^{-35} \lambda^3 n_e^2 T_e^{-1/2}, \tag{5}$$

where λ is the wavelength of laser in μm. The photoionization absorption coefficient α_{pi} estimated with Kramers' formula is[45]

$$\alpha_{PI} = 7.9 \times 10^{18} \left(\frac{E_n}{h\nu}\right)^3 \left(\frac{I}{E_n}\right)^{\frac{1}{2}} \sum_n N_n, \tag{6}$$

where λ is the laser wavelength E_n and N_n are the ionization energy and number density of the excited state n, h is Planck's constant, ν is the laser frequency, and I is the ionization potential of the ground state atom. The photoionization absorption coefficient is obtained by summing up all the excited states levels whole ionization energy is smaller than the laser photon energy. Considering the high photon energy of 266 nm laser photons ($h\nu = 4.6$ eV), the photoionization will be the major absorption mechanism at UV wavelengths, while because of λ^3 dependence IB absorption will be dominant at IR wavelengths. Chang and Warner reported domination of photoionization over IB absorption at higher laser intensities for visible wavelength excitation.[45]

Numerous studies have been conducted to quantify and qualify the effects of differing absorption processes on laser induced plasmas. The details of the implications IB and PI absorption processes on laser induced plasmas can be found in Refs. 16, 19, 30, and 46. Mao *et al.*[47] attributed different mass ablation rates for 1064 nm, 532 nm, and 266 nm laser wavelengths to plasma shielding occurring as a result of IB processes dominant at longer wavelengths. Bogaerts *et al.*[16] incorporated photon absorption coefficients into their numerical model of laser ablation and induced plasma formation to properly describe laser absorption in the plasma at varying wavelengths. Typically for metals the leading mechanism for plasma ignition is inverse bremsstrahlung leading to cascade-like growth of electron density. Hence the plasma ignition thresholds will be lower for IR wavelengths than UV even though enhanced laser-target coupling is expected at lower wavelengths.[43]

Both shadowgraphy and fast photography have been used routinely for analyzing laser ablation plumes in the presence of ambient gas. Russo and co-workers[33,34] investigated thoroughly the role of background gas on expansion dynamics of laser ablation plumes by solving conservation equations of mass, momentum, and energy and predicted the propagation of internal and external shock waves and contact surface and compared with experimental results obtained from shadowgraphy and emission images. Their results highlight the role of background gas atomic mass on laser-plasma coupling. Recently, Harilal *et al.*[12] studied the main features of plume expansion in ambient Ar using shadowgraphy and fast gated self-emission imaging and found expansion dynamics as well as shock structure of the plasma plume can be reproduced using a continuum hydrodynamics model. The shape of the plasma plume, the pressure and position of shock front were found in good agreement with the experimental results. The initial-stage asymmetric expansion, the internal shock-wave-like plume structure, and the vertical motion were also observed in their studies.

Both shadowgraphic and self-emission images showed rapid expansion in the first 10–20 ns followed by slow propagation. However, a comparison between the time sequence of shadowgraphic and ICCD images and their position-time plots showed distinct dissimilarities. The R-t plots obtained using shadowgraphic images followed classical blast wave model, with a best fit for shorter wavelengths and lower energies. Conversely, ICCD images showed plume confinement, indicated by less extension of the plume length compared to shadowgraphy images. Previous studies showed the self-emission from the plasma due to target bulk atoms/ions moves more slowly than the plume-ambient boundary, which does not generate any visible emission aside from refractive changes in the medium.[12]

The time resolved electron density estimate showed similar trends for all Nd:YAG laser wavelengths, although consistently higher values were noticed for UV laser ablation. The electron density of 1064 nm produced plasma gave the lowest values while 266 nm gave higher values. Hoffmann *et al.*[19] compared the role of laser wavelength on space resolved electron density of carbon plume and reported slightly higher densities for shorter wavelength generated plasma and which they explained as due to enhanced ablation rate at shorter wavelength. This conclusion is consistent with reported mass ablation rate which followed a $\lambda^{-4/9}$ dependence with wavelength,[48] as well as deeper craters observed for shorter wavelength excitation. As discussed before, enhanced plasma screening at longer wavelengths reduces the laser-target coupling leading to shallower craters for IR wavelengths compared to UV irradiation.

Apart from laser absorption by the sample, the amount of laser energy effectively coupled to the target also depends on target reflectivity[16]

$$E \sim I_o(1-R)(1-A), \tag{7}$$

where I_o, R, and A are laser irradiance at the target surface, target reflectivity, and % of absorption by the plasma reflectivity, respectively. This equation indicates that target reflectivity may affect the effective laser-target coupling. However, the reported Al metal reflectivity for 266 nm, 532 nm, and 1064 nm differ only slightly, given as 0.92, 0.92, and 0.95, respectively.[49] Hence, it is likely that plasma absorption mechanisms are responsible for the different ablation rates of 266 nm, 532 nm, and 1064 nm laser excitation wavelengths over aluminum. Bogaerts and Chen[16] studied the effects of 1064 nm, 532 nm, and 266 nm wavelengths on a copper target in one atmosphere helium gas using a comprehensive computational model. Their model showed little difference between 266 nm and 532 nm crater depths, which they attributed to the balancing of target reflectivity and plasma shielding effects at 532 nm.[16] Presently, we are working on modeling of laser ablation plumes and the effect of excitation wavelength on plasma dynamics in the presence of ambient gas using HEIGHTS simulation package[23,50] and the results will be published in a future article.

V. CONCLUSIONS

We investigated the role of laser wavelength on plasma expansion and confinement at atmospheric pressure. The plasmas are generated using fundamental, second, and fourth harmonics of Nd:YAG laser wavelength and analyzed using various plasma diagnostic tools. The use of multiple experimental techniques provided a comprehensive view of various processes involved in laser-target coupling and laser-plasma generation, and their dependence on excitation laser wavelength. Shadowgraphy and fast photography provided important information about the hydrodynamic expansion of shock wavefronts and plasma plumes. Shadowgraphic images at the early times of plume generation highlight the role of laser wavelength on plasma generation and supported the hypothesis that inverse Bremsstrahlung is the dominant absorption mechanism at 1064 nm. Plume structures were observed as cylindrical for IR wavelengths and spherical for UV laser excitation. The position-time plots obtained using shadowgrams followed classical spherical blast wave model for all wavelengths of excitation studied, however, a noticeable departure from spherical geometry is evident at higher energies, especially for IR wavelength. The position time plot obtained from self-emission images showed higher confinement of plasma plumes in ambient pressure compared to shadowgraphy data.

Optical emission spectroscopy provided important information about the electron number density of plasmas during plume expansion. Time resolved electron density data showed sudden decrease at times <100 ns, irrespective of the laser excitation wavelength used. It was found that for all energies investigated, 266 nm pulses had the highest densities over all at times studied and 1064 nm provided the lowest electron densities. This is due to differences in laser-target and laser-plasma coupling at different wavelengths. Analysis of crater profiles using white-light interferometry showed that the deepest crater depths were obtained shorter wavelengths compared to IR wavelength. It is likely that differing plasma absorption mechanisms for the three wavelengths are responsible for varying ablation rates over aluminum. The use of several experimental techniques in this work was very useful in forming a cogent description of the effect of laser wavelengths on laser produced plasmas.

ACKNOWLEDGMENTS

This work was supported by the US DOE National Nuclear Security Administration under Award No. DE-NA0001174.

[1]A. W. Miziolek, V. Palleschi, and I. Schechter, *Laser-Induced Breakdown Spectroscopy (LIBS): Fundamentals and Applications* (Cambridge University Press, Cambridge, UK, 2006).
[2]J. P. Singh and S. N. Thakur, *Laser-Induced Breakdown Spectroscopy* (Elsevier, Amsterdam, 2007).
[3]R. W. Coons, S. S. Harilal, S. M. Hassan, and A. Hassanein, Appl. Phys. B **107**, 873 (2012).
[4]R. E. Russo, X. L. Mao, O. V. Borisov, and H. C. Liu, J. Anal. At. Spectrom. **15**, 1115 (2000).
[5]R. R. Gattass and E. Mazur, Nature Photon. **2**, 219 (2008).
[6]K. F. Al-Shboul, S. S. Harilal, and A. Hassanein, Appl. Phys. Lett. **100**, 221106 (2012).
[7]D. B. Chrisey and G. K. Hubler, *Pulsed Laser Deposition of Thin Films* (John Wiley & Sons, New York, 1994).
[8]M. Crank, S. S. Harilal, S. M. Hassan, and A. Hassanein, J. Appl. Phys. **111**, 033301 (2012).
[9]J. R. Freeman, S. S. Harilal, B. Verhoff, and A. Hassanein, Plasma Sources Sci. Technol. **21**, 055003 (2012).
[10]D. W. Hahn and N. Omenetto, Appl. Spectrosc. **64**, 335A (2010).
[11]J. F. Ready, *Effects of High-Power Laser Radiation* (Academic, New York, 1971).
[12]S. S. Harilal, G. V. Miloshevsky, P. K. Diwakar, N. L. LaHaye, and A. Hassanein, Phys. Plasmas **19**, 083504 (2012).
[13]S. S. Harilal, C. V. Bindhu, M. S. Tillack, F. Najmabadi, and A. C. Gaeris, J. Appl. Phys. **93**, 2380 (2003).
[14]S. S. Harilal, B. O'Shay, Y. Tao, and M. S. Tillack, J. Appl. Phys. **99**, 083303 (2006).
[15]A. De Giacomo, M. Dell'Aglio, R. Gaudiuso, S. Amoruso, and O. De Pascale, Spectrochim. Acta, Part B **78**, 1 (2012).
[16]A. Bogaerts and Z. Y. Chen, Spectrochim. Acta, Part B **60**, 1280 (2005).

[17]D. Breitling, H. Schmittenhelm, P. Berger, F. Dausinger, and H. Hugel, Appl. Phys. A **69**, S505 (1999).
[18]R. Fabbro, E. Fabre, F. Amiranoff, C. Garbanlabaune, J. Virmont, M. Weinfeld, and C. E. Max, Phys. Rev. A **26**, 2289 (1982).
[19]J. Hoffman, T. Moscicki, and Z. Szymanski, Appl. Phys. A **104**, 815 (2011).
[20]D. Campos, S. S. Harilal, and A. Hassanein, J. Appl. Phys. **108**, 113305 (2010).
[21]D. Campos, S. S. Harilal, and A. Hassanein, Appl. Phys. Lett. **96**, 151501 (2010).
[22]I. H. Hutchinson, *Principles of Plasma Diagnostics* (Cambridge University Press, New York, 2002).
[23]S. S. Harilal, T. Sizyuk, A. Hassanein, D. Campos, P. Hough, and V. Sizyuk, J. Appl. Phys. **109**, 063306 (2011).
[24]M. Polek, S. S. Harilal, and A. Hassanein, Appl. Opt. **51**, 498 (2012).
[25]A. Kumar, R. K. Singh, J. Thomas, and S. Sunil, J. Appl. Phys. **106**, 043306 (2009).
[26]T. A. Schmitz, J. Koch, D. Gunther, and R. Zenobi, J. Appl. Phys. **109**, 123106 (2011).
[27]S. Amoruso, C. Aruta, P. Aurino, R. Bruzzese, X. Wang, F. M. Granozio, and U. Scotti di Uccio, Appl. Surf. Sci. **258**, 9116 (2012).
[28]C. Sanchez-Ake, M. Bolanos, and C. Z. Ramirez, Spectrochim. Acta, Part B **64**, 857 (2009).
[29]S. S. Harilal, J. Appl. Phys. **102**, 123306 (2007).
[30]N. M. Shaikh, S. Hafeez, B. Rashid, and M. A. Baig, Eur. Phys. J. D **44**, 371 (2007).
[31]B. Verhoff, S. S. Harilal, J. Freeman, P. K. Diwakar, and A. Hassanein, J. Appl. Phys. **112**, 093303 (2012).
[32]M. A. Shannon, X. L. L. Mao, A. Fernandez, W. T. Chan, and R. E. Russo, Anal. Chem. **67**, 4522 (1995).
[33]S.-B. Wen, X. Mao, R. Greif, and R. E. Russo, J. Appl. Phys. **101**, 023114 (2007).
[34]S. Wen, X. Mao, R. Greif, and R. E. Russo, J. Appl. Phys. **101**, 023115 (2007).
[35]T. A. Schmitz, J. Koch, D. Guenther, and R. Zenobi, Appl. Phys. B **100**, 521 (2010).
[36]Y. B. Zel'dovich and Y. P. Razier, *Physics of Shock Waves and High-Temperature Hydrodynamic Phenomena* (Dover Publications, Inc., Mineola, New York, 2002).
[37]T. Y. Choi and C. P. Grigoropoulos, J. Appl. Phys. **92**, 4918 (2002).
[38]H. R. Griem, *Principles of Plasma Spectroscopy* (Cambridge, New York, 1997).
[39]N. Konjevic, A. Lesage, J. R. Fuhr, and W. L. Wiese, J. Phys. Chem. Ref. Data **31**, 819 (2002).
[40]G. Cristoforetti, S. Legnaioli, V. Palleschi, E. Tognoni, and P. A. Bendetti, J. Anal. At. Spectrom. **23**, 1518 (2008).
[41]Q. Ma, V. Motto-Ros, F. Laye, J. Yu, W. Lei, X. Bai, L. Zheng, and H. Zeng, J. Appl. Phys. **111**, 053301 (2012).
[42]J. Y. Gravel and D. Boudreau, Spectrochim. Acta B **64**, 56 (2009).
[43]L. M. Cabalin and J. J. Laserna, Spectrochim. Acta B **53**, 723 (1998).
[44]S. Amoruso, M. Armenante, V. Berardi, R. Bruzzese, and N. Spinelli, Appl. Phys. A **65**, 265 (1997).
[45]J. J. Chang and B. E. Warner, Appl. Phys. Lett. **69**, 473 (1996).
[46]A. Bogaerts, Z. Y. Chen, R. Gijbels, and A. Vertes, Spectrochim. Acta B **58**, 1867 (2003).
[47]X. L. Mao, A. C. Ciocan, O. V. Borisov, and R. E. Russo, Appl. Surf. Sci. **127–129**, 262 (1998).
[48]R. A. Burdt, S. Yuspeh, K. L. Sequoia, Y. Z. Tao, M. S. Tillack, and F. Najmabadi, J. Appl. Phys. **106**, 033310 (2009).
[49]W. M. Haynes, *CRC Handbook of Chemistry and Physics* (CRC Press, Boca Raton, FL, 2013).
[50]A. Hassanein, T. Sizyuk, V. Sizyuk, and S. S. Harilal, J. Micro/Nanolith. MEMS MOEMS **10**, 033002 (2011).